Encapsulation of hexylsalicylate in an animal-free chitosan-gum arabic shell by complex coacervation

Baiocco, Dan; Preece, Jon; Zhang, Zhibing

DOI:
10.1016/j.colsurfa.2021.126861

Document Version
Peer reviewed version

Citation for published version (Harvard):
Baiocco, D, Preece, J & Zhang, Z 2021, 'Encapsulation of hexylsalicylate in an animal-free chitosan-gum arabic shell by complex coacervation', *Colloids and Surfaces A: Physicochemical and Engineering Aspects*, vol. 625, 126861. https://doi.org/10.1016/j.colsurfa.2021.126861

Encapsulation of Hexylsalicylate in an Animal-Free Chitosan-Gum Arabic Shell by Complex Coacervation

Daniele Baiocco[a], Jon A. Preece[b] and Zhibing Zhang[a*✉]

[a] School of Chemical Engineering, University of Birmingham, Edgbaston, Birmingham, B15 2TT, UK

[b] School of Chemistry, University of Birmingham, Edgbaston, Birmingham B15 2TT, UK

[*✉] Z.Zhang@bham.ac.uk; D.Baiocco@bham.ac.uk;

***Abstract* — Fabrication of oil (hexylsalicylate) encapsulated microcapsules comprising a shell of gum Arabic and fungal chitosan *via* complex coacervation was investigated herein. This study highlights the influence of the fabrication conditions including the ratio of gum Arabic to chitosan, their zeta-potential and turbidity on the physico-mechanical properties of the resulting microcapsules. Glutaraldehyde was employed as a chemical cross-linking agent. Three states of the capsules were characterised namely, moist, air-dried and spray-dried using several analytical techniques (SEM, TEM, FTIR, and UV-Vis spectrophotometry). Moreover, the microcapsules were assayed for their mechanical properties including rupture force, nominal stress at rupture, and nominal deformation at rupture, which were determined to be 2.0 ± 0.1 mN, 3.6 ± 0.3 MPa, and 22.7 ± 1.5 %, respectively. An encapsulation efficiency (~60%) of the oil-based active ingredient and an oil leakage rate (<10% after one month) in water environments were determined. Such promising results suggest the above mentioned vegetable chitosan-gum Arabic system to be a potential carrier for the encapsulation of fragrance ingredients, which presents a new opportunity to globally overcome cultural and religious concerns associated with animal sourced products.**

***Keywords* — Perfume Microcapsules, Complex Coacervation, Chitosan, Zeta-Potential, Micromanipulation, Animal-free.**

1. INTRODUCTION

Fragrances are currently added to many consumer products, such as laundry and personal care products, to aid the consumer perception of cleanliness and freshness to encourage consumer repeat purchase [1, 2]. Fragrances are volatile organic compounds (VOCs) which may be chemically reactive, and therefore, if incorporated directly into a formulated product would be prone to evaporating during storage and/or react with other formulated ingredients [3, 4]. Therefore, strategies to inhibit fragrance evaporation and chemical degradation in formulated products are desired, as they allow reducing the amount of fragrance required in the product, which reduces cost of manufacture, as well as enhancing the consumer experience, subsequently leading to an increasing revenue. To this end microencapsulation, first pioneered by Bungenberg de Jong's in 1929, has been used to encapsulate VOCs leading to (i) reduced oil volatility in formulated products, and (ii) partitioning from the rest of the formulation reducing cross-reactivity with other actives. Thus, microencapsulation has enabled a reduction in the overall amount of fragrance required to deliver a positive consumer experience [5]. Furthermore, the microcapsules containing the fragrance act as delivery vehicles, by physically attaching themselves to clothe or hair fibres during a wash, and then when dried will not release the fragrance until mechanical action breaks the microcapsules, *e.g.* wearing of a garment or running fingers through hair [6], resulting in a much enhanced customer experience of cleanliness and freshness from hours to days post-wash. For such applications, it is crucial for the fabricated microcapsules to have optimum mechanical strength and very low leakage rate of the actives in aqueous environment. In order to encapsulate fragrance molecules (or flavour ones) to protect them from other actives in a formulation, several methods have been developed and reviewed [7]. Among the physico-mechanical microencapsulation techniques, such as extrusion and solvent evaporation [8], spray drying has been found to be both the highest yielding and quickest method to produce powders with encapsulated flavours from oil-in-water emulsions [9]. Meanwhile, a few chemical approaches have been used, including *in-situ* polymerisation [10], molecular inclusion [11], co-crystallisation [12], and coacervation [13] in order to encapsulate fragrances and flavours. Coacervation methods provide high payloads, as well as mechanically tuneable microstructures, and has gained much interest as a VOC microencapsulation process [14]. Coacervation refers to the self-assembly of macromolecules at an oil-aqueous interface to give colloidal systems (colloidosomes) [15]. More specifically, suspended biopolymer-based solids combine into a concentrated colloidal phase, the coacervate, which is separated out of a much diluted colloidal system [16]. Non-soluble biopolymer-derived complexes naturally settle down within the medium, thereby resulting in a phase-separated mixture [17]. The phase separation, as well as the ensuing dynamic deposition of the colloidosomes layering up around a non-miscible core, can be triggered either by a single colloidal species or multiple biopolyelectrolytes consisting in simple or complex coacervation, respectively [18]. Strictly depending upon the hydration level of the reacting medium, simple coacervation (SC) could be physically developed when a single-colloid solution is enriched with a very hydrophilic ingredient, resulting in two separated phases being the colloidal-abundant and colloidal-depleted ones [19].

Alternatively, Dickinson & Galazka [20] have described complex coacervation (CC) as a naturally occurring phase

conversion into two immiscible phases consisting of a biopolymer-rich phase and solvent-poor phase with precipitated biopolymer. Furthermore, solution pH and electrostatic interactions between oppositely charged biopolyelectrolytes must be controlled in order to effectively drive CC phenomena [15]. The optimum conditions for CC may be easily identified as the oppositely charged polyelectrolytes approach their isoelectric point and exhibit the highest degree of electrostatically interacting polyions carrying opposite charges, therefore, maximising binding *via* salt bridges [21]. Espinosa-Andrews *et al.* (2013) have suggested that an accurate zeta-potential analysis of the biopolymer stock solutions might provide crucial information about colloid stability in terms of the pH in order to maximise the electrostatic interactions between the two co-polymers. Relying on pH control, a similar approach was applied to a different bi-polymeric system consisting of gelatine (Gl) and gum Arabic (GA). The results revealed that an effective neutralisation of the overall opposite charge density, causing the formation of strong polyionic bonds, could be achieved [22].

In recent years, attention has been drawn to a few protein-polysaccharide systems including soybean, as well as pea-protein isolate-chitosan (Ch) [23, 24], silk-fibroin-Ch, *beta*-lactoglobulin-Ch [25], whey protein-GA [18, 26], and how the main process conditions affected the chemical interactions mainly responsible for the complex coacervation [16].

Several polysaccharide-polysaccharide systems including Gl-GA and GA-Ch pairs have been investigated [27]. The former is one of the most effective pairs in the fabrication of core-shell microstructures, whereas the latter is less well studied [28]. The authors have suggested that GA and Ch may result in attractive interplays when CC is driven under specific pH conditions. As such, Ch has been reported as a potential candidate for CC owing to its dual electrostatic identity. More specifically, Ch carries positive charges at slightly acidic pH values below its own pK_{aCh} (6.2-7) which is associated with the protonation of Ch's glucosamine units [15, 23, 29]. GA has been suggested as a potentially suitable match to Ch at pH values above its pK_{aGA} (~2.2) since negative charges are borne, by the carboxylates [30, 31]. Furthermore, both biopolymers exhibit highly appealing properties encompassing biodegradability and biocompatibility. GA is naturally secreted as a gummy glue-like exudate derived from *Acacia Senegal* [32], and has been globally accepted because of its high solubility in water with moderate viscosity levels, and its remarkable emulsifying and shell-forming properties [15]. Ch is a widely available and environment-friendly biomaterial typically synthesised by alkaline deacetylation of chitin from crustaceans and insects' exoskeletons [33, 34]. However, the main drawback associated with this type of Ch and Gl is that they are derived from animal sources, whilst consumers are increasingly demanding for solely plant-based ingredients [22, 27, 35]. Furthermore, animal sourced ingredients can have allergen proteins, non-negligible heavy metal concentrations, and health-compromising pollutants, which are coming under regulatory control [3, 36]. Therefore, ambitious efforts have been recently launched to formulate animal-free alternatives. Interestingly, fungally produced Ch (fCh), which is typically produced *via* solid-state fermentation from *Aspergillus niger* [37], has arisen as a potential candidate to be matched against GA in CC [38]. Interestingly, fCh derivatives have been found to provide promising physico-chemical properties when compared to materials currently employed in microencapsulation, such as marine Ch and Gl obtained from swine/bovine hide [38]. However, there is no literature report on

the potential of fCh as a microencapsulating agent, and there is no information on the mechanical and structural properties of fCh-based microcapsules. Therefore, the application of fCh as a microencapsulating agent could pave the way for the replacement of animal sourced Ch microcapsules, as they are more consumer-friendly having less trace allergens, metals and pollutants [38, 39]. In addition, fCh being acceptable to vegetarians and vegans [38], is more easily accessible for formulation into products, as extraction from the fungal ferment is relatively facile and green [40], compared to the extraction of Ch from the animal derived materials [41, 42]. The work presented here is aimed at the encapsulation of a key fragrance oil component (hexylsalicylate (HS)) by inducing CC on a fully animal-free GA-fCh system. In addition, the physico-chemical and mechanical properties of these microcapsules, their encapsulation efficiency, payload and release rate in aqueous environment were characterised using scanning electron microscopy (SEM), Fourier transform infrared spectroscopy (FTIR), micromanipulation, and UV-Vis spectrophotometry, and the results are herein presented.

2. MATERIALS AND METHODS

2.1 Materials

Gum Arabic (InstantGum Acacia AA) and food-grade animal-free fungal Chitosan, fCh, (molecular weight <190 kDa, degree of deacetylation (DDA) 80%, KiOsmetine-Cs®) were provided by Nexira Food (Rouen, France, EU) and Kitozyme S.A. (Herstal, Belgium, EU), respectively. All the solutions were prepared using deionised water (18.2 $M\Omega \cdot cm^{-1}$ at 25 °C). Liquid Nitrogen (ℓ-N_2) was generously donated by the Birmingham Centre for Energy Storage (BCES, Birmingham, UK).

All other analytical-grade reagents including hexylsalicylate (>99.0 %, density = 1.04 $g \cdot mL^{-1}$), 1-octanol (~99 %), sorbitan trioleate (Span85), triethanolamine (TEA), fuming hydrochloric Acid (36 % w/v HCl), sodium hydroxide (NaOH), potassium bromide (KBr), LR white acrylic resin and 50% (w/w) aqueous glutaric aldehyde (Glu) were purchased from Sigma-Aldrich (Dorset, UK), stored by following the Safety Data Sheet (SDS) guidelines, and used without further purification.

2.2 Biopolymer stock solution preparation

fCh-based aqueous stock solutions (100 mL, 2.0 % w/w) were prepared by adding powdered fCh (2g) into deionised water whilst stirring with a Rushton turbine (ϕ 38 mm) mounted on an overhead stirrer (IKA, Germany) operating at 400 rpm, followed by the addition of aqueous HCl (0.1 N, approx. ~3 drops) to adjust the pH from 5.5 to 4.0 (pH probe in solution). Stirring was continued for 30 min to afford a slightly turbid dispersion. GA aqueous stock solution (100 mL, 1.0 % w/w) was prepared by adding the powdered GA (1g), over 20 min, into deionised water, with stirring as for fCh, to afford a clear solution having a pH ~6. A combined stock solution (CSS) consisting of both fCh (65 mL) and GA (65mL) stock solutions was prepared by adding GA solution to fCh solution, over 1 minute whilst stirring (Rushton turbine) at 400rpm, and then stirring was

continued for a total of 20 min affording the CSS a slightly turbid dispersion with pH_{CSS} ~5.2. All solutions were maintained at 25±0.3°C using double-glazed 250 mL jacketed reactors equipped with 4 baffles and connected to a circulating water bath (Grant R-1, Grant Instruments, UK).

2.3 Microcapsules synthesis *via* CC

Additional fCh (0.95 g) was added over 5 minutes to CSS (130 mL) whilst stirring at 400 rpm, and then stirring was continued for a total of 25 min, after which a more turbid dispersion resulted. Additional GA (14.35g) was added over further 20 minutes, whilst stirring at 400 rpm, and then stirring was continued for a total of 45 min at 400 rpm (ω_{CSS}). The addition of fCh, as for GA, was carried out over 5 minutes and 20 minutes, respectively, because aggregate grains of the powdered materials would adhere to the air-water (a-w) interface, if added too quickly. The resulting turbid dispersion with a GA-to-fCh weight ratio equal to 6.7 was acidified to pH 1.95 (Figure 1 - Step 1) by adding HCl_{aq} (36% w/v, (~0.6mL)). Such acidification resulted in a rapid reduction in turbidity and formation of a clear solution. The solution was stirred at 400 rpm for 30 min, at which point there was a foam at the a-w interface. The stirring was then stopped. Consequently, around 0.4mL of 1-octanol (defoaming agent) was added to deplete the foam at the a-w interface. The resulting solution (CSS*) was left to rest for 15 min.

HS (40g) was added to the CSS* over 2 minutes (Figure 1 – Step 2) forming two phases. An emulsifying agent, Sorbitan triolate (Span85, 0.8 g), was added *via* a disposable syringe (5mL, Emerald, Becton Dickinson S.A., Spain, EU), in order to produce a kinetically stable oil-in-water (o/w) emulsion (Span85-to-HS weight ratio 0.02 (g Span85)·(g-HS)$^{-1}$). The mixture was homogenised at 1000 rpm ($\omega_{o/w}$) with an overhead stirrer (Microstar 7.5, IKA, Germany, EU) for 30 min in order to form an o/w emulsion (Figure 1 – Step 3). The size of the resulting emulsified droplets, which are directly related to the stirring rate [43, 44], was measured by means of a particle sizer (Malvern Mastersizer, UK). Oil droplets with a volume-based mean size of around 30 μm were achieved under stirring at 1000 rpm. The emulsion was allowed to stabilise for 30 min (emulsion stabilisation time) under continuous stirring (1000 rpm) to lower the interfacial tension and its resulting interfacial energy, hence increasing the stability of emulsion itself [45]. No variation in the droplet mean size (~30 μm) was detected by particle sizer after 30 min [46]. The stirring speed was progressively reduced (over 5 min) to 0 rpm. The resulting o/w emulsified mixture was found to be forming a whitish froth build-up at the a-w interface, which was the result of pockets of air naturally entrapped in the liquid phase due to the earlier continuous emulsification at 1000 rpm. Thus, 1-octanol (~0.2 mL) was added which spread onto the a-w interface using the tip of a transfer pipette to reduce/eliminate froth. Subsequently, the o/w emulsified CSS* was transferred into a double-glazed jacketed 2L reactor (equipped with 4 baffles and coupled with a temperature-controlled water circulator thermostated at 25±0.3°C (Model F33-HL, Julabo GmbH, Germany, EU)) containing deionised (600 mL) water at pH 1.95, which had been pre-acidified *via* dropwise addition of HCl_{aq} (36% w/v). At this point, CC phenomena between fCh and GA were induced under stirring (ω_{CC}: 400 rpm or 1000 rpm) by dropwise addition of a TEA_{aq}

solution (2% w/w, 160 mL) by means of a motorised syringe pump (Harvard Apparatus, US) operating at a controlled flow rate (2mL·min^{-1}). The infusion of 2% (w/w) aqueous TEA was carried out over 80 minutes because clusters of coarcevates would occur if the pH was rapidly increased. Therefore, progressive addition of the aqueous TEA solution to the emulsified CCS* led to a gradual pH increase (Figure 1 – Step 4).

The progression of CC (*i.e.* the formation of the shells *via* CC around the oil droplets) was monitored by an optical microscope (Leica DM500, USA) by taking out samples at every 0.1 unit increase of the medium pH measured with a pH meter with a resolution ±0.01 units (Model FP20, Mettler Toledo, UK). The infusion of the aqueous TEA solution was stopped once the typical CC shell structure encircling each oil droplet had become visible by optical microscopy. The stirring rate was gradually reduced (over 5 min) down to 300 rpm, which was applied for further 20 minutes. At this point, the resulting microcapsules were inspected again by optical microscopy to check for the successful formation of the shell around the oil droplets. 5.0 g of aqueous glutaric aldehyde (50% w/w) was added (over 2 min) to allow the freshly formed microcapsules to crosslink for ~20 hours at 40±0.3°C under continuous stirring at 300 rpm (ω_{CL}) (Figure 1 – Step 5). Three samples of crosslinked microcapsules in the resulting suspension were immediately taken out and assayed for particle size analysis. The main steps (1–5) of the microencapsulation process are displayed in Figure 1.

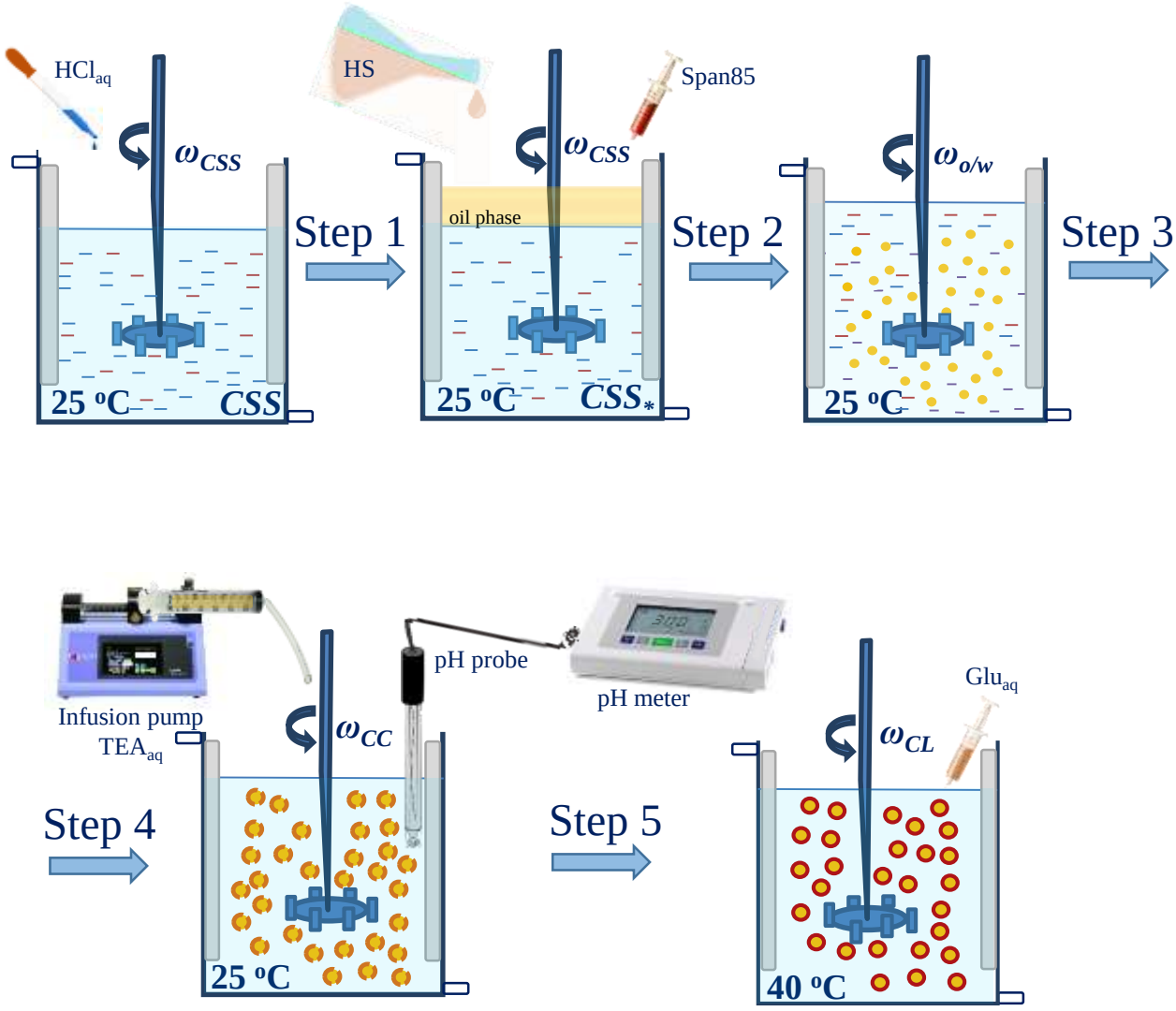

Figure 1 – Schematic diagram of the encapsulation process of HS *via* CC within a fCh-GA based shell: biopolymeric dispersion with a GA-to-fCh weight ratio equal to 6.7 and pH 1.95 (Step 1); gradual addition of HS and Span85 (Step 2); emulsification step at stirring rate of 1000 rpm for 30 min in order to form o/w droplets (Step 3); gradual infusion of the 2% (w/w) TEA aqueous solution into the emulsified CCS* at 25±0.3°C to induce CC phenomena (Step 4); crosslinking stage by addition of 50% (w/w) aqueous Glu at 40±0.3°C (Step 5). Top/Bottom rectangles (▭) represent the inlet/outlet of the jacketed reactor. Vertical grey bars represent the baffles. Red and blue dashes represent fCh and GA in solution, respectively (Step 1-2-3); yellow spheres represent the emulsified oil droplets (Step 3); dashed orange and solid red annuli represent the freshly formed and crosslinked shells, respectively (Step 4-5).

2.4 Analytical Techniques

2.4.1 Net electrokinetic charge (NEC) and Zeta-potential (ζ) of biopolymer stock dispersions

Zeta-potentiometry was used to measure the net electrokinetic charge of a polymer in each stock solution using the Nano ZS90

(Malvern, UK) operating at ambient temperature. The equipment's software benefitting from Smoluchowsky's mathematical theory is enabled to convert electrophoresis-based measurements into NEC (soluble polymers) or ζ-values (colloidal dispersions) [47]. More particularly, the light beam travelling throughout each sample detects orientation and velocity of the electrically oriented polyelectrolyte dispersions when an electrostatic field is being applied. The remaining GA (1.0% (w/w)) and fCh (2.0% (w/w)) stock solutions (35 mL each) were transferred into two separate airtight vials covered with aluminium foil, and temporarily left at ambient temperature for no longer than two hours prior to zeta-potential measurement. Subsequently, each 35mL stock solution was divided into ten 3.5 mL aliquots. The pH of each 3.5mL aliquot was manually adjusted *via* acidic and alkaline titration (using 0.1N aqueous HCl and 0.1N aqueous NaOH) to cover the pH range 1.0-8.0, which must include both pK_{afCh} and pK_{aGA}. When dealing with fCh, the pH values as measured by a pH meter were 1.12, 1.96, 2.78, 3.01, 4.02, 4.29, 4.67, 5.67, 6.50, and 7.98. The pH 6.50 aliquot was prepared to monitor the behaviour of the NEC of fCh around its own pK_{afCh} (~6.0-6.5). In addition, the pH 3.01 aliquot was utilised 5 times, initially, as such, at pH 3.01 and then by addition of NaOH to raise the pH to 3.25, 3.42, 3.73, 3.92 to achieve four additional measurements between pH 3-4, where Espinosa-Andrews *et al.* [28] showed the highest NEC for Ch. As for fCh, the pH values for GA, as measured by the pH meter, were 1.10, 1.80, 2.05, 2.23, 3.10, 4.10, 5.14, 6.32, 7.03, and 7.95. The pH 1.80 and 2.23 aliquots were prepared to monitor the behaviour of the NEC of GA around its own pK_{aGA} (~1.8-2.2). 0.5 mL from each aliquot was diluted into 4.5mL of HCl_{aq}/$NaOH_{aq}$ with the same pH as each aliquot. The folded capillary zeta measurement cell (plastic cuvette (capacity ~0.8 mL), DTS1070, Malvern, UK) was thoroughly rinsed three times with deionised water (18.2 MΩ·cm^{-1}), prior to being inoculated with any fCh/GA aliquot to be measured.

2.4.2 Turbidity Studies

The aliquots which had been previously prepared for the NECNEC/zeta potential analysis (1:10 dilution) were utilised for the turbidity measurements of fCh and GA to cover the same pH range (1.0-8.0). The turbidity of fCh and GA samples at different pH values was measured to investigate how the turbidity of fCh/GA dispersion occurs at different pHs. A benchtop turbidity meter (HI-93703, Hanna Instruments, UK) specially designed for maintaining the required wavelength (peaking at 890 nm) and passing a beam of infrared (IR) light through 25-mm round glass vials was calibrated with the aid of three reference standards, and employed to measure each aliquot. The 90°-scattered light was detected by a built-in light sensor, quantified by a microprocessor displaying the readings in Formazine Turbidity Units (FTU), which can be converted into mg SiO_2·L^{-1} (FTU/ mg·L^{-1} ≃ 0.13) or into ppm (ρ_{sol} ≃ 1 g·mL^{-1}). The data collected from the turbidity studies were then associated with that from the ζ-potential measurements, in order to investigate any potential interrelationship between turbidity and the electrostatic charge of the biopolymers at different pHs.

2.4.3 Fourier Transform Infrared Spectroscopy (FT-IR) of powdered GA, fCh and GA-fCh microcapsules

Both GA and fCh dry powders were used without any further treatment. The suspension containing HS-entrapping microcapsules with a GA-fCh based shell was spray-dried by means of a spray dryer (B-290 mini, Büchi, Switzerland) to achieve a free flowing powder of microcapsules for FT-IR tests. The spray dryer was coupled with a peristaltic pump feeding the suspension into the main cylindrical chamber through a 1.5-mm wide nozzle, and operated at 160 °C until approximately 3 g of powder was yielded. FT-IR spectra of all solid samples were obtained employing a FT-IR GX System (Perkin-Elmer, US) paired with an attenuated total reflection (ATR) sampling accessory (DuraSampleIR device, US). All spectra were given as an average of 200 scans from 4000 to 400 cm^{-1} (wavenumber) at a resolution of 4.0 cm^{-1}. Solid powders (7.5 mg) were gently mixed and contained within an IR-transparent anhydrous KBr (0.5 g) based matrix acting as a window material, and then compressed (force applied 80 kN for 120 s) into pellets using a semi-automatic rotary tablet press equipment with a pellet-forming die (LFA Tablet Presses, UK). The sample-to-KBr weight ratio equal to 0.015 was selected to prevent the formation of opaque pellets which may undesirably result in little IR beam passing throughout the pellets, hence generating poor IR response.

2.4.4 Particle Size Analysis

A particle size analyser (Mastersizer 2000, Malvern Instruments Ltd., UK) equipped with a continuously stirred sample dispersing unit (CSSDU) (Hydro2000SM, Malvern Instruments Ltd., UK) was used to investigate the mean size, as well as size distribution of the microcapsules. 5 mL of suspended HS-microcapsules were transferred in the CSSDU (2000rpm) containing ~120 mL of deionised water, and then analysed. The results obtained are the average of five consecutive measurements, with two-minute interval. The instrument was aligned using an effective refractive index ($\widetilde{RI}$) resulting from a weighted average (Eq.1) of the individual *RI* values of GA (RI_{GA} ~ 1.476) and fCh (RI_{fCh} ~ 1.521) equal to 1.482. The refractive index of HS was RI_{HS} 1.505. $D_{[3,2]}$ is the Sauter mean diameter (Eq. 2) while the size distribution is characterized by the SPAN value (Eq. 3) [44, 48]:

$$\widetilde{RI} = \beta \cdot RI_{Ch} + (1 - \beta) \cdot RI_{GA} \quad (1)$$

$$D_{[3,2]} = \frac{\sum_{i=1}^{N} d_i^3}{\sum_{i=1}^{N} d_i^2} \quad (2)$$

$$SPAN = \frac{d_{90\%} - d_{10\%}}{d_{50\%}} \quad (3)$$

where β is derived from the weight fraction of GA and fCh; d_j represents the diameter of individual microcapsules, N refers to

the total number of microcapsules being measured; $d_{10\%}$, $d_{50\%}$, $d_{90\%}$ are the diameter of particles when the cumulative volume fraction is caught at 10%, 50% and 90%, respectively.

2.4.5 Morphology Characterisation

The morphology of microcapsules was firstly assessed *via* an optical microscope. Secondly, around 0.1 mg of spray-dried microcapsules per sample were gently tapped onto a stainless steel stub equipped with a conductive double-sided adhesive carbon tab as a substrate. Subsequently, the microcapsules were covered through gold sputtering (Polaron Sputter Coater SC7640 equipped with a valve-controlled argon cylinder, Quorum Technology Ltd, UK) to create an electrically conductive coating of gold onto the sample (~8 nm), in order to avoid charging effects, and to best exploit the high resolution features of a high-vacuum scanning electron microscope (SEM, JEOL 6060, USA) operating under accelerating voltages (15-30 kV). The thickness of the Au-coating was monitored by means of a thickness monitor coupled with a quartz crystal (QC) holder mass monitoring device. Moreover, the shell thickness of microcapsules was preliminarily evaluated by SEM imaging on microcapsules which had been frozen by liquid N_2, and ground in an agate pestle and mortar to mechanically cause structural damage.

2.4.6 Encapsulation Efficiency and Payload

UV-Vis measurements were performed to evaluate both encapsulation efficiency (EE) and payload of microcapsules by using a standard calibration curve. Three 50 mg specimens of spray dried microcapsules were first loaded into three different screw capped bottles, and then dispersed into 50 mL of 36% (w/w) aqueous propanol ($PrOH_{aq}$) as a receptor medium according to Mercade-Prieto, Allen [5]. The bottles were placed in an ultrasonic water bath (VWR Ultrasonicator, USC100TH, UK) for 30 min at ambient temperature in order to extract the core material (HS) which had been retained within the fCh-GA coacervate shell. Following the ultrasonication, damaged microcapsules/shell residues occurring in the aqueous medium were separated out by centrifugation (Hermle Labortechnik Z-180, Labnet, Germany, EU) at 1900 g-force for 5 min to afford a clear HS-containing supernatant. The absorbance of the supernatant was measured by a UV-Vis spectrophotometer (CE 2021, Cecil Instruments Ltd., UK) which had been zeroed on a blank sample (36% (w/w) aqueous propanol). UV-Vis measurements were recorded according to the peak absorbance wavelength of HS (λ_{HS} = 306 nm) [5]. The supernatant was diluted in a quartz cuvette 10 times using the blank sample prior to measurement. The amount of HS was calculated using a standard HS *vs* 36% (w/w) propanol calibration curve (coefficient of determination $R^2 > 0.98$). All measurements were performed in triplicate. Both $EE_{\%}$ (Eq. 4) and $Payload_{\%}$ (Eq. 5) were evaluated with the following formulae:

$$EE_{\%} = \frac{m_a}{m_{TL}} \cdot 100 = \frac{\frac{m_{core}}{m_{sample}}}{1 + \frac{m_{s,EN}}{m_{c,EN}}} \quad (4)$$

$$Payload_{\%} = \frac{m_{core}}{m_{sample}} \cdot 100 \quad (5)$$

where m_{core} represents the mass of core material in microcapsules; m_{sample} is the mass of the sample; $m_{s,EN}$/ $m_{c,EN}$ is the weight ratio of the amount of shell to core materials used for encapsulation; m_a and m_{TL} are the actual and theoretical loadings of the oil, respectively.

2.4.7 Release Profile Studies

Core material release studies were performed at ambient temperature by exposing microcapsules to aqueous environments according to Mercade-Prieto *et* al. [5]. 1.0 mg of spray-dried microcapsules were weighed and placed inside a dialysis tube (length ~5 cm, internal diameter ~14.3 mm, molecular weight cut-off (MWCO) 12-14 kDa, visking code DTV12000, Medicell Membranes Ltd, UK) which had been formerly soaked into deionised water at 60 ^{o}C for 3 hours, and then thoroughly rinsed with deionised water (25 ^{o}C) in order to remove the glycerol coating. The edges of each tube were folded twice, and secured by applying lab pegs at either end. Each tube containing HS-microcapsules was immersed in 50mL of the selected receptor medium, which was deionised water (DI-w), and continuously stirred with a magnetic flea. Aliquots (3mL) were sampled every 10 minutes within the first hour; every 30 minutes within the second and third hour; every 60 minutes until the sixth hour. Afterwards, the release of HS was monitored on the daily basis within the first week, and then observed on the weekly basis until a plateau release value was evident. Following each withdrawn aliquot, the same volume (3mL) of fresh DI-w solution was promptly replaced in the appropriate receptor medium in order to assure the sink condition. UV-Vis spectra of each sample were recorded, and the typical absorption band of HS peaking at 306 nm was measured. Each data set was processed using the appropriate HS calibration curve obtained with DI-w. All experiments were carried out in triplicates.

2.4.8 Micromanipulation

The mechanical properties of microcapsules were determined using a micromanipulation technique relying on compression of singularly selected microparticles/microcapsules [49-52]. The schematic of the micromanipulation rig previously presented by Zhang *et al.* (1999) is displayed in Figure 2. A small amount of microcapsules suspended in water (two droplets) were left drying in air on a thin pre-cut glass slide (~2.5 cm^2). The glass slide was placed beneath a glass probe (original diameter 1 mm) with a tapered tip having flat end of 70μm (total length 0.8 cm), which had been polished against a fine lapping film (1 μm) mounted on a high-speed rotary polisher (Model EG-40, Narishige, MicroInstruments Ltd., Long Hanborough, UK). The resulting polished tip was longitudinally mounted onto the output borosilicate glass based tube (outer diameter 1 mm, inner

diameter 0.58 mm; Harvard Apparatus Ltd, Kent, UK) of a selected force transducer (Model 403A, maximum force scale 5 mN, Sensitivity 0.453 $mN \cdot V^{-1}$, Aurora Scientific Inc., Canada) being coupled with an electrically driven control box. The force transducer was attached to a three-dimensional micromanipulator controlled by a servo motor (Parker Compumotor, USA). The vertical direction was adjusted by means of a motor responsible for both moving distance and speed. The glass slide was fixed onto a metal stage, and the compression process was monitored by a side-view camera being focused on the selected particle and connected to a monitor (Figure 2 – TV monitor side view). At least 30 microcapsules occurring on the glass slide were selected and compressed to rupture. Each microcapsule was squashed out at a compression speed of 2.0 $\mu m \cdot s^{-1}$, and both force output and displacement data were filed. Compliance of the system was run 3 times prior to each test, and their average value was used to calculate the real displacement of the force probe.

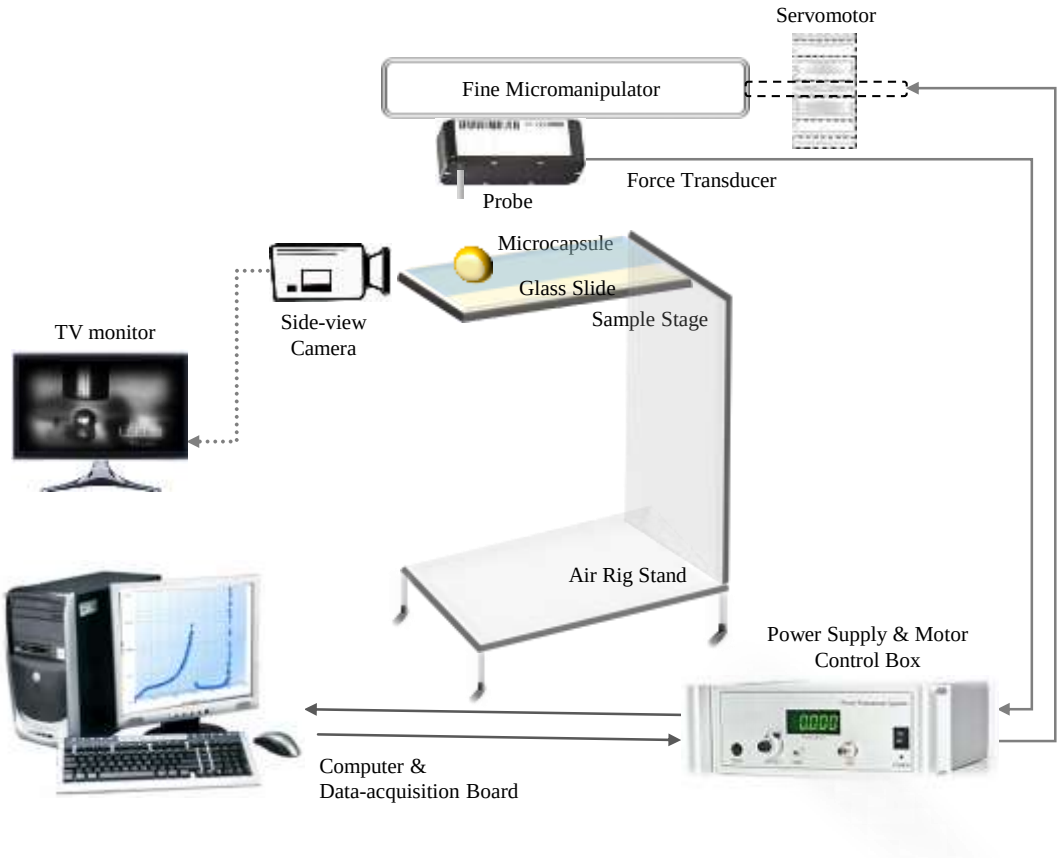

Figure 2 – Schematics of the micromanipulation rig. Both computer screen and TV monitor depict what is being displayed during a typical compression test of a single microparticle/microcapsule.

3. RESULTS AND DISCUSSION

3.1 Net electrokinetic charge (NEC) and Zeta-Potential

The trend of NEC as a function of the pH is displayed in Figure 3A, for both fCh and GA solutions. All aqueous fCh solutions/dispersions showed non-negative NEC values over the selected pH range (1.0-8.0). The most positive value of fCh approximately equal to +65 mV was obtained at pH 3.4. The typical positive charge is ascribable to the protonation of glucosamine segments ($NH_2 + H^+ \rightleftarrows NH_3^+$) occurring at pH<5.5-6.0, which corresponds to its $pKa_{,fCh}$ [42]. Interestingly, the positive charge of fCh was found to drop dramatically at any pH above ~5.5-6.0 since protonation of fCh's glucosamine segments is severely impaired at near-neutral pHs [53]. Particularly, this behaviour has been associated with the deprotonation of the ammonium groups $NH_3^+ \rightleftarrows NH_2 + H^+$ resulting in loss of positive charge [42]. Also, this phenomenon has been tentatively related with the coil conformation of chitosan, which is extended only at low acidic pHs due to strong segment-segment repulsion phenomena [28, 54, 55].

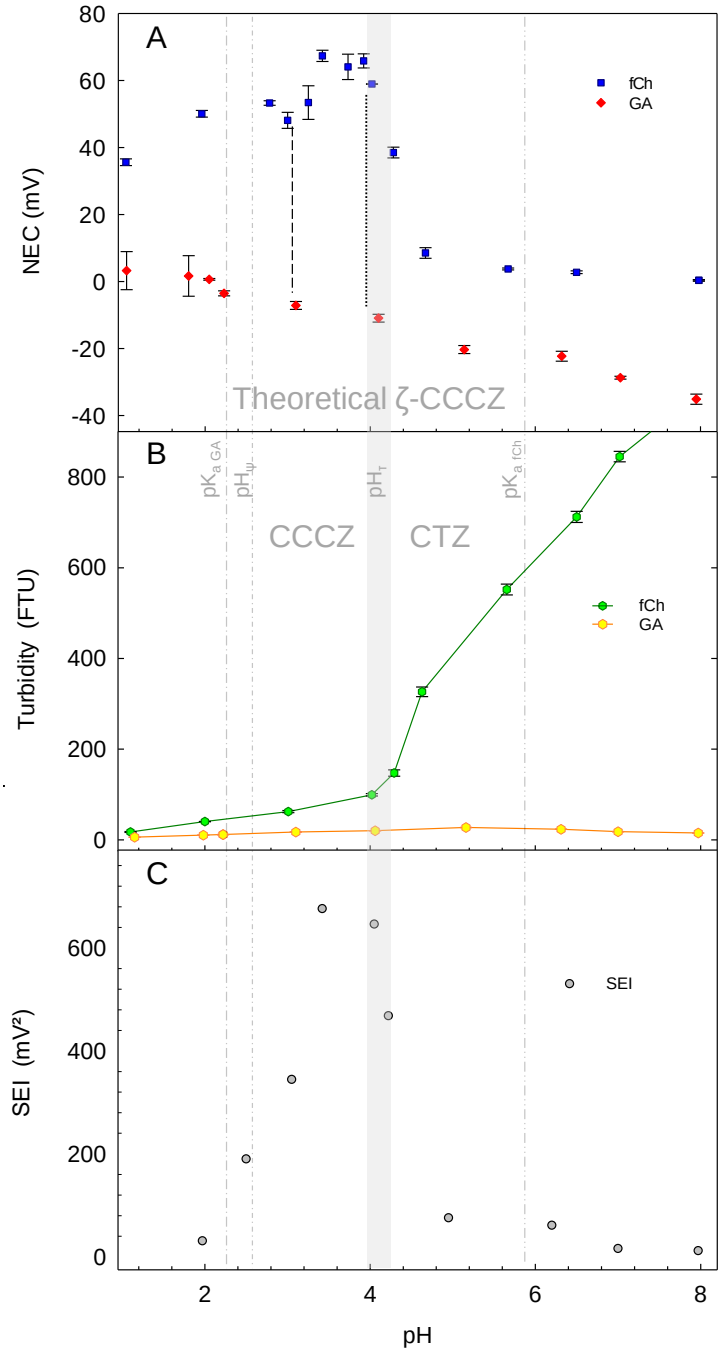

Figure 3 – Net electrokinetic charge (NEC) of soluble biopolymers or ζ-potential of biopolymer dispersion (A) and turbidity (B) of fCh/GA solutions/dispersions with the strength of electrostatic interaction (SEI) (C) at different pH values. The resulting theoretical NEC/zeta-potential Complex Coacervation Comfort Zone (ζ-CCCZ) solely based on the NEC measurement is displayed between $pK_{a\,GA}$ (·—·) and $pK_{a\,fCh}$ (··—··); the operative CCCZ is displayed between pH_{ψ} (·-·) and the left edge of pH_{τ} (grey bar) since the critical turbidity zone (CTZ) occurs at pH ≥ pH_{τ}; pH_{τ} represent the solubility-to-insolubility transition area of fCh. Error bars may be smaller than the size of the symbols.

Moderately acidic fCh-based dispersions (pH 4.3) were found to develop a slightly turbid appearance (Figure 4B), whereas highly acidic fCh dispersions (pH 1.1) turned completely clear (Figure 4A). Previous literature has suggested that chitosan solubility is conditional upon the distribution of N-acetyl and free amino functional groups (NH_2) in the glucosamine units

[56]. Protonation of amino groups into NH_3^+ was observed at pH below 6.0 (~pK_{aCh}) due to which Ch/fCh had become partly soluble [42]. Clear fCh solutions are triggered, at highly acidic pH, by the distribution of active NH_3^+ units naturally available below its own pKa_{fCh}, which are thus responsible for the degree of solubility of fCh in aqueous media. Therefore, turbid dispersions of fCh observed at pH values above its $pKa_{,fCh}$ (Figure 4C) would contain a large distribution of non-protonated amines resulting in fCh insolubility. As for animal-derived Ch, no fCh is expected to electrostatically interact with any oppositely charged species (*e.g.* GA) above its $pKa_{,fCh}$ [57]. When dealing with GA, non-positive NEC values were exhibited by GA solutions between pH 2 and 8, whereas cautiously weak cationic charges were detected for GA at pH 1.0-2.0 (Figure 3A). Previous literature confirmed that GA is always negatively charged in solution having pH above 2.0 [58]. The interrelationship between the charge nature of GA and the pH is governed by the deprotonation mechanism of GA's carboxylic moieties ($COOH \rightleftarrows COO^- + H^+$), which is associated with its pKa_{GA} occurring at pH 1.8-2.2 [59]. Accordingly, a charge switchover point for GA was clearly identified at pH ~ 2.1-2.2 where its electrostatic charge was found to be transitioning from a weakly positive value to increasingly negative values, as also reported by Dong and Hua [60]. The overall charge distribution of GA progressively became more and more negative as the pH was increased, with a value equal to –35.1 mV following alkalinisation to pH~8.0. The results were found to be in good agreement with the data previously presented for GA by Weinbreck *et al*. [18], Espinosa-Andrews *et al.* [28] , and Dong and Hua [61] . However, several values measured for GA were determined to be slightly different from those provided by Jiménez-Alvarado *et al.* [62]. Most likely, such discrepancies might result from differences in the nature, purity, ageing, chemical composition, and dispensing stage of the raw ingredient supplied. Strength of Electrostatic Interaction (SEI) is displayed in Figure 3C. SEI is a parameter derived as the absolute value of product between the zeta potential values (or NEC charge) of both oppositely charged polyelectrolytes taken at a specific pH [18, 28]. As such, SEI values being pH-dependent are meaningful over the pH range where biopolymer pairs only exhibit opposite charges, and hence attractively interplay with each other [18]. As shown in Figure 3C, this range was found to occur between pH ~2.2 and ~6.0 for the GA-fCh system. More particularly, the greatest SEI value (677 mV^2) for the GA-fCh system was determined between pH 3.0 and 4.0. Overall, SEI should be considered as a theoretical electrostatic indicator to tentatively suggest the pH region where the interactions between GA and fCh are maximised, thereby promoting their mutual charge neutralisation. Therefore, a net pH-triggered charge neutralisation between two biopolymers carrying opposite charges would result in CC phenomena [63]. Besides, CC occurring at the maximised attractive interaction point of two biopolymers bearing opposite charges may not only lead to the separation of coacervates, but also to robust structures as benefitting from the strongest possible interplays. When all involved ion *vs* counter-ion charges (carried by fCh and GA) actively interact with each other at the most favourable pH, the fCh-GA system triggered the most compact complexes. This behaviour has also been reported for chitosan-GA systems by Vuillemin *et al.* [64]. Moreover, the same authors have suggested that the effectiveness of strong Ch-GA is greatly influenced by the steric hindrance of Ch itself, which is beneficially reduced at specific temperature and pH conditions.

Figure 4 – Bright-field microscopy imaging of fCh-based aqueous dispersions at different pH values: clear and translucent at pH 1.1 with fully dissolved fCh (A), slightly turbid with non-fully dissolved fCh at pH 4.3 (B), and highly turbid and non-translucent due to non-dissolved fCh at pH 8.0 (>pK_{afCh}) (C). The vials show the appearance of the fCh-based aqueous dispersions at the pH values displayed.

Interestingly, a theoretical NECNEC/zeta-potential Complex Coacervation Comfort Zone (ζ-CCCZ) based on the electrostatic interactions between GA and fCh can be introduced. This indicator is shown in Figure 3 between pK_{aGA} and pK_{afCh}, thereby encompassing the whole pH region within which only opposite charges are borne by the biopolymers. ζ-CCCZ is aimed at identifying all theoretical pH matches which may induce coacervation between two oppositely charged biopolymers, such as fCh and GA. As displayed in Figure 3B, the lower bound pH value of ζ-CCCZ referred to the GA-fCh system was determined to be pH_{ψ} 2.5. pH_{ψ} value has been experimentally validated as the starting point of phase separation phenomena of GA and fCh by CC, at which GA-fCh based coacervates were first observed to begin separating out and, in turn, encircling the oil droplets (Figure 5A). Alternatively, the upper bound pH value was associated with pKa_{fCh} (~6.0) since no clear formation of the intact shells *via* CC around single oil droplets was observed (Figure 5C). Hindered CC phenomena were probably due to the cationic charge drop of fCh at pH~ pKa_{fCh}. Moreover, no significant CC at pH~pKa_{fCh} appeared consistent with the extremely low SEI values exhibited by the fCh-GA system at pH≥pKa_{fCh}. As previously mentioned, poor/no solubility of fCh in aqueous media with near-neutral (~6.0-6.5) as well as alkaline pH (>7) leads to no CC phenomena because no protonation of fCh's amine moieties occurs above pKa_{fCh} [42]. As expected, non-protonated fCh resulted in highly turbid fCh dispersions, which were observed at slightly basic pH ~ 8.0 (Figure 4C). In addition, slightly turbid dispersions observed at pH~4.0-4.3 (Figure 4B) suggest the incipiently impaired solubility of fCh in water (due to partially protonated glucosamine units), which may tentatively identify the solubility-to-insolubility transition area of fCh, *i.e.* pH_{τ} [53]. Notwithstanding, the establishment of an *a-priori* ζ-CCCZ relying on the mere electrostatic analysis may only be utilised as a guideline to preliminarily attempt CC-suitable matches between pairs of biopolymers bearing opposite charges within a specific pH range. Overall, ζ-CCCZ does not directly involve any turbidity implications, hence extra endeavours were undertaken by this research team to interrelate the NEC/zeta-potential analysis with the turbidity related studies.

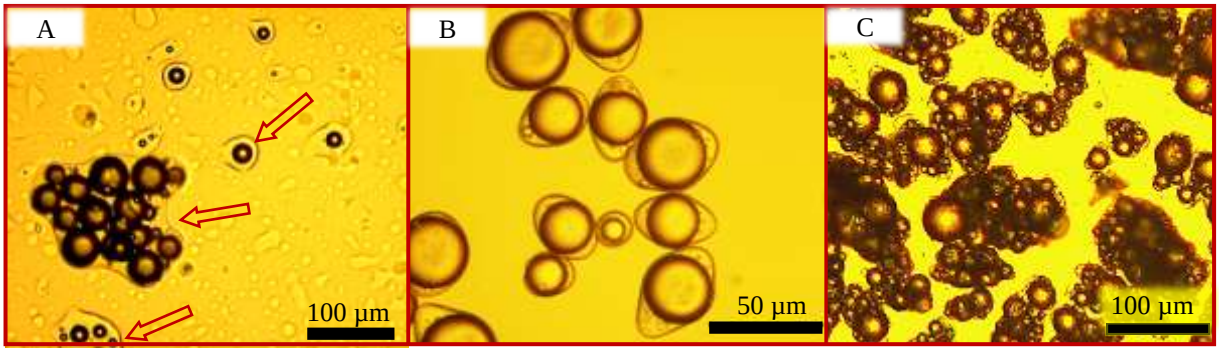

Figure 5 – Optical microscopy imaging of (A) incipient formation of shells entrapping single/multiple oil droplets *via* CC (pH 2.5, T = 25.0 ˚C) imaged by optical microscopy; (B) eye-shaped microcapsules synthesised *via* CC with a core of HS (pH 3.4, T = 25.0 ˚C); (C) no clear formation of the intact shell *via* CC around single/multiple oil droplets (pH 6.0, T = 25.0 ˚C).

3.2 Turbidity

Turbidity is defined as the cloudiness of a dispersion due to non-dissolved colloidal matter [65]. As explained by Davies-Colley and Smith [66], this phenomenon directly targets solid particles which are likely to scatter a light beam passing through the dispersing medium. Information relating to the turbidity of the fCh-GA system was collected, and then interrelated with the ζ-potential analysis (Figure 3A-B). The turbidity *versus* pH of GA and fCh is shown in Figure 3B. As can be seen, fCh exhibited a moderate rise in turbidity from 15 to 150 FTU when the pH was increased from 1.1 to 4.3 (*i.e.* right edge of pH_{τ}), which is consistent with what are shown in Figure 4A-B. Moreover, similar results have been reported by Geng *et al.* [67] suggesting that chitosan may be from partly to completely dissolvable when exposed to slightly and highly acidic media, respectively. As the pH was increased above pH_{τ}, a surge in the turbidity level of fCh solutions was observed. Interestingly, the turbidity level of fCh at pH 5.5 was determined to be around 4-fold higher than that observed within pH_{τ}. The appearance of fCh dispersions became more and more turbid when the pH was adjusted from slightly acidic to neutral/alkaline, which is reflected in the exponential-like boost in fCh's turbidity curve presented in Figure 4B. These findings are in agreement with what was previously observed from the ζ-analysis since no highly positive ζ-values had been determined for fCh at and above pH~5. As formerly mentioned, this phenomenon could be ascribable to fCh adopting a non-extended conformation at weakly acidic pHs and above (≥5.5-6.0) probably due to the depleted glucosamine segment-segment repulsion, resulting in a lower intrinsic viscosity of fCh itself [15, 54]. The net increase in turbidity of fCh dispersions under non-optimal dissolution conditions is attributed to the cationic charge loss of the glucosamine units along fCh's chains (Hudson and Jenkins, 2001). Thus, limited/no occurrence of free positive charges around fCh's glucosamine units would lead to limited/no electrostatic phenomena [42]. Moreover, the increase in turbidity could be taken as a physical evidence of fCh possessing a non-extended conformation at weakly acidic pH and above [42]. As reported for animal chitosan, non-extended conformations of Ch, at

weakly acidic pHs and above, have also been associated with its semicrystalline nature due to inter- and intra-molecular hydrogen bonds, which trigger insolubility [68]. In addition, previous literature suggests that the flexibility of chitosan's reactive moieties along its chains may be enhanced at pH ~ 3, thereby maximising the protonation of its own available glucosamine units [69].

Alternatively, the turbidity of GA solutions exhibited minor variations over the investigated pH range (1-8) with typical values ranging between 5 and 30 FTU. This finding was expected since GA is well known to be highly water soluble [70]. Overall, the turbidity data suggests that well-dissolved fCh-GA-based mixtures should be achieved exclusively at highly acidic pH values ($<pH_{\tau}$) where very low turbidity levels of both biopolymers were observed. Besides, the vertical gap between the turbidity curves of both GA and fCh increased mildly below pH_{τ}, whereas a much higher gap was observed above pH_{τ}. When comparing GA/fCh turbidity curves with each other, fCh could be appointed as the dominant material in terms of turbidity and dissolvability in water, while GA only plays a supplementary role. Also, the interrelationship between pH-dependent turbidity and ζ-potential plots led to further findings. Given that the greatest biopolymer-to-biopolymer electrostatic interaction was determined *via* SEI to fall between pH 3.0 and 4.5, any pH higher than pH_{τ} and below pK_{afCh} would hit the increasingly high turbidity zone of fCh. Thus, poor CC due to fCh may be expected within its high turbidity zone. Interestingly, a critical turbidity zone (CTZ), spotlighting high turbidity zone for the investigated biopolymeric system (fCh-GA) can be individuated. CTZ is displayed between pH_{τ} and pK_{afCh} in Figure 3B. Notwithstanding that fCh and GA bear positive and negative charges at pHs lower and higher than their own pKa values (pK_{afCh} ~5.5-6.0; pK_{aGA} ~ 1.8-2.2), respectively, the previously identified theoretical ζ-CCCZ should be then reduced in width due to the turbidity of fCh occurring at and above pH_{τ}. More specifically, the former ζ-CCCZ should be narrowed down between pH_{ψ} and the left edge of pH_{τ} (~4.0) to hit a turbidity-free zone, which is CCCZ (Figure 4B). Thus, CCCZ also includes the turbidity effects on the solubility/reactivity of the biopolymers. In addition, the derivative of SEI was determined to be positive and steep between pH 2.2 and 3.5 ($\partial SEI/\partial pH > 0$), evidencing the increase in the strength of the electrostatic interaction between GA and fCh. Basing on the highest SEI value obtained, the most theoretically desirable pH for CC (pH_{CC}) between fCh and GA should be around 3.4-3.5, at which the most effective neutralisation of their opposite charges is anticipated. Overall, the establishment of CCCZ paired with CTZ may be considered as a useful approach for predicting suitable biopolymer pairs to chemically react *via* CC within their most convenient turbidity-free pH range.

3.3 Determination of the optimum CC ratio

The optimisation of the processing conditions is crucial to achieve microcapsules with desirable physio-chemical and mechanical properties. Particularly, the biopolymer-to-biopolymer ratio can be determined by comparing the NEC trends of each biopolymer occurring in the turbidity-free CCCZ [22]. Specifically, several straight lines being perpendicular to the pH axis are contained within the CCCZ. The vertical dashed line originating through pH 3 hits the NEC curves of fCh and GA

exhibiting charges of around +54.2 mV and -7.3 mV, respectively (Figure 3A). Similarly, the dotted line through pH 4 shows the NEC of fCh and GA solutions to be +59.1 mV and -9.3 mV, respectively. As presented, in both cases (pH 3 and pH 4), the absolute NEC of fCh were found to be very different when compared to GA, and vice versa. Therefore, the vertical lines originating from the NEC values of each biopolymer through a given pH were quantified in order to identify a biopolymer-to-biopolymer weight ratio suitable for CC between GA and fCh. There appeared to be required non-equal amounts of each biopolymer to compensate the electrostatic gap between GA and fCh, thereby enabling their charge neutralisation effectively [22]. Accordingly, a greater amount of GA would be needed to promote full neutralisation of all counter-ions carried by fCh. Basing on the concentrations adopted, the vertical gaps taken at pH 3 and 4 suggest that the amount of GA to employ should be stoichiometrically within six to seven-fold higher than fCh. Particularly, the highest NEC value between GA and fCh was detected at pH 3.4 ($\zeta_{fCh,max}$ = +67.9 mV; $\zeta_{GA,max}$= –9.9 mV) with a globally maximised SEI = 677 mV^2. The corresponding GA-to-fCh weight ratio at pH 3.4 was 6.7 (m_{GA} / m_{fCh} = 15 g GA / 2.25 g fCh). The formation of coacervate shells around the individual oil droplets was seamlessly achieved at pH 3.4 (Figure 5B) where attractive interactions between GA and fCh are maximised. Thus, pH 3.4 has been adopted as an optimum completion pH_{CC} between GA and fCh. These findings were found to be in very good agreement with former literature suggesting that the highest cationic charge of chitosan, and hence the strongest protonation of the amine groups on its chains, occurs at pH 3.6 [27], which is also reflected on its total conductivity [71]. Further studies conducted by Butstraen and Salaün [27] have also shown that pH 3.6 was required for triggering CC between chitosan and GA at the maximum of their electrostatic interaction (*i.e.* zero-charge/equivalence point). Overall, the amounts of biopolymers to react *via* CC need to be adjusted in order to neutralise the oppositely charged ammonium and carboxylate functional groups carried by Ch/fCh and GA, respectively [22].

3.4 Morphology

SEM images of dried HS-entrapping microcapsules are presented in Figure 6. An overview of the microcapsules is displayed in Figure 6A. It can be observed that the microcapsules were relatively spherical with a moderately rough surface (Figure 6B). The presence of significant surface pores might have been due to the extreme vacuum conditions resulting in the typical liquid-puffing phenomenon (Figure 6H), which had been extensively investigated by Farshchi *et al.* [72]. The microcapsules were found to be highly sensitive to high vacuum as well as prolonged electron beam exposure due to which structural damage of microcapsules and, thus and oil leakage, were observed (Figure 6C-D). Interestingly, eye-shaped microcapsules were obtained by moderate stirring (400 rpm) (Figure 6E); alternatively, more spherical microcapsules were obtained at 1000 rpm (Figure 6F). At the lower stirring speed, the oil droplets/microcapsules were larger on average (Figure 7), which means their corresponding specific surface area (surface area per volume) was smaller. Consequently, there would be more shell materials available for coating each oil droplet. Therefore, the excess amount of the shell materials could be deformed around the oil droplets by the agitation during the solidification, thereby generating eye-shapes shells. Similarly, elongated shapes were also

reported by Leclercq *et al.* [73] for gelatine-based microcapsules by CC. The mean diameters of the microcapsules prepared at 400 rpm and 1000 rpm were 50±2 μm and 35±1 μm, respectively. At the higher speed, the oil droplets were expected to be smaller, and the effect of their interfacial tension with the continuous phase was more significant to minimise their surface area, resulting in more spherical droplets, then microcapsules. The shell of a randomly selected cryo-damaged microcapsule is also presented in Figure 6G. Interestingly, there appeared that the shell of such HS-entrapping microcapsules may be several hundred nanometers thick.

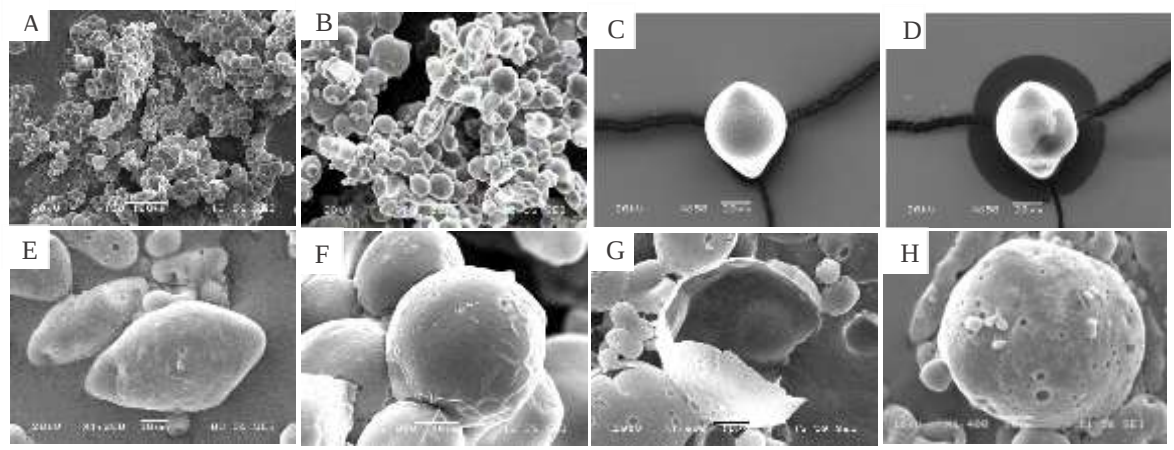

Figure 6 – SEM images of dried HS-entrapping microcapsules with different magnifications being ×370 (A) and ×100 (B); foreground images of a dried microcapsule exposed to high vacuum conditions before (C) and after leaking (D); effect of the stirring rate on microcapsules obtained at 400 rpm (E) and 1000 rpm (F); shell thickness of a cryo-damaged microcapsule (G) and multiple surface pores possibly due to liquid puffing from microcapsules (H).

3.5 Size and Size Distribution

The size distribution of HS-entrapping microcapsules obtained at 400 rpm was determined to be reasonably narrow (SPAN = 1.23), ranging between 20 and 117 μm together with a mean Sauter mean diameter of 50±2 μm (Figure 7). As expected, HS-entrapping microcapsules obtained at a higher stirring speed (1000 rpm) were determined to have a narrower size distribution (SPAN = 0.94), varying from 15 to 78 μm with a mean diameter $D_{[3,2]}$ of 35±1 μm. In addition, accurate statistical analysis highlights that a Gaussian distribution can be plausibly fitted to the size distribution of the microcapsules with 95% confidence. The mean size as well as the size distribution of the moist microcapsules obtained by means of the particle analyser was proven to be well consistent with their SEM micrographs (Figure 6).

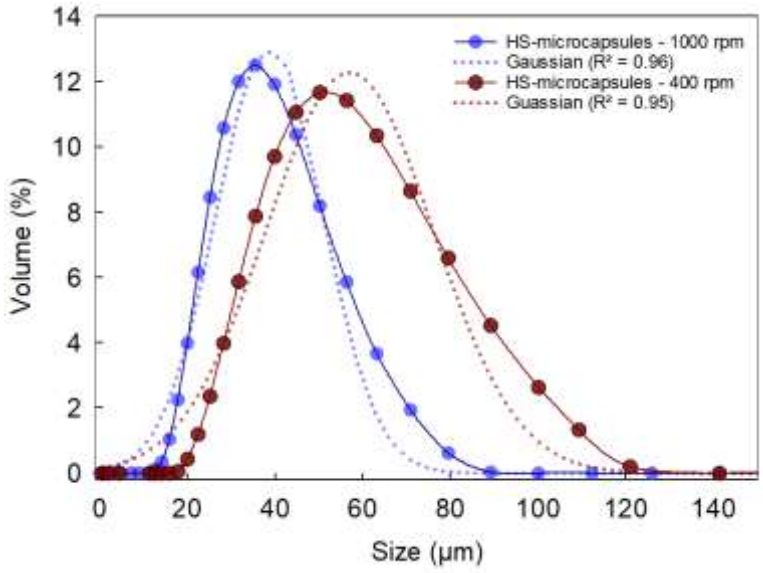

Figure 7 – Size distribution of moist HS-entrapping microcapsules obtained at 400 rpm (red) and 1000 rpm (blue).

3.6 Functional Groups Interrelationship (FT-IR analysis)

GA and fCh powders, HS as well as HS-entrapping microcapsules were all assayed for their FTIR spectra. An observation of fCh's spectrum (Figure 8α) highlights a broad vibrational band occurring at 3383 cm^{-1}, which is related to the amino-hydroxyl ($–NH_2$ –OH) moieties. A characteristic band found at 2893 cm^{-1} was obvious and ascribable to the vibration of C–H bond [23, 74]. A few more bands peaking at 1681, 1595, 1303 cm^{-1} were detected and tentatively associated with the stretching vibration of the double-bounded C=O segment occurring in the acetylated groups ($–CONH_2$), the amide III units ($–NH_3^+$) [10], and the synergic effect due to –CH and –OH, respectively [75]. Furthermore, the symmetrical stretching vibration of C–O–C and the stretch absorption of C–O could be read at 1159 and 1036 cm^{-1}, respectively. The typical absorption bands of GA are displayed in Figure 8β. Specifically, the –OH-related stretching vibrations could be identified at 3340 cm^{-1}. Another absorption band was evident at 1610 cm^{-1}, which was attributable to the conjugated C=C units. Furthermore, the non-symmetrical as well as symmetrical vibration of the carboxylated ions ($–COO^–$) was detected in the region of 1290 cm^{-1}. Similarly to fCh, a 1033cm^{-1} peak was found to be corresponding to C–O-unit stretching [76]. Figure 8γ displays the FTIR spectrum of HS. Specifically, the strong band appearing at 1720-1630 cm^{-1} was assigned to the typical stretching vibration of the double-bounded C=O segment of aromatic carboxylic esters [77]. Similarly, the bands located at 1230-1140 cm^{-1} and 1120-1020 cm^{-1} were related to the stretching of C–C–O and O–C–C groups of the saturated ester [78]. Moreover, the peaks at 2954 cm^{-1} and 2864 cm^{-1} were ascribable to the aromatic and alkyl C-H stretching, respectively. The FTIR spectrum of tableted HS-microcapsules is shown in Figure 8δ. The band visible around 3280cm^{-1} was ascribable to the stretching vibration of amine ($–NH_2$) and hydroxyl (–OH) groups. When comparing Figure 8α-8β with 8δ, it could be deduced that a significant modification of the FTIR spectrum occurred in HS-microcapsules due to the presence of the fCh-GA shells. This phenomenon was also reflected in the presence

of broader peaks assigned to the carbonyl-amide region (1650-1300cm^{-1}), possibly suggesting the successful electrostatic interplays between the $–NH_3^+$ segments of fCh and the $–COO^–$ of GA [74]. Besides, Kildeeva *et al.* have also reported the formation of azomethine groups (Schiff base) in the region of 1680–1620 $cm^{–1}$ [79], which cannot be excluded following CC. Other peaks were also obvious at 3315 $cm^{–1}$ as well as 3159 $cm^{–1}$, 1406 $cm^{–1}$, and 1033 $cm^{–1}$, which were cautiously associated with the stretching vibrations of amino($–NH_2$)-hydroxyl(–OH) groups, alcoholic segments (–OH), amino-acid zwitterions exhibiting a C=O group, and C–O units, respectively. Furthermore, a narrow peak possibly indicating the development as well as the stretching of vinyl groups ($–CH=CH_2$) was also detected at 920 $cm^{–1}$. The absorbance peak occurring at 611$cm^{–1}$ may suggest the stretching vibration of N–H. However, it may also indicate the establishment of a new chemical segment attributable to the side formation of chloro-alkanes, since HCl had been employed to adjust the pH in the process. In addition, a moderately broad absorbance peak detected at 1033 $cm^{–1}$ may be due to the major vibrational stretching of alcoholic segments. Overall, these peaks were found to be in agreement with what reported by Espinosa-Andrews *et al.* [74]. Additionally, the comparison between Figure 8γ and 8δ highlighted that no strong signal associated with HS was detectable in the tableted HS-microcapsules. This phenomenon may be due to HS being screened out by the encapsulating polymeric matrix made of fCh and GA. Therefore, the spectra of fCh (Figure 8α) and GA (Figure 8β) seemed much similar to that of HS-microcapsules (Figure 8δ). However, Figure 8δ also exhibited two relatively broad bands with sharp peaks at 1400-1200 cm^{-1} and 750-600 cm^{-1}. Since these peaks were not observed from 8α and 8β, they could be likely attributed to some weak interference due to presence of sub-shell oil (HS) in the HS-microcapsules. In addition, this finding may also provide indirect information on the shell thickness of HS-microcapsules, given that the depth of penetration of FTIR measurements is typically in the micron range. Having said that, the shell thickness should be in the range of several hundreds of nanometres and the FTIR penetration depth itself, following the very weak signal attributable to HS in the FTIR spectrum of HS-microcapsules. This observation was consistent with the SEM micrograph presented in Figure 6G.

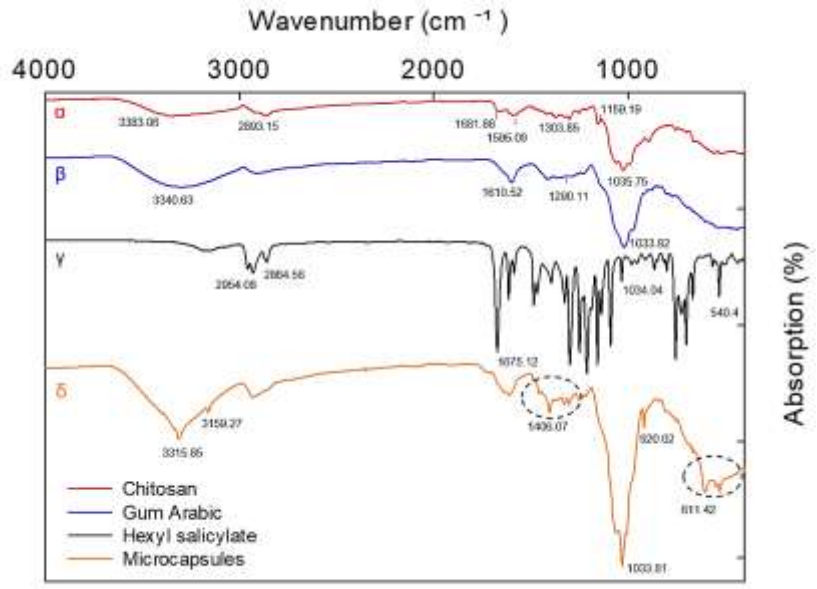

Figure 8 – FT-IR spectra of solid Ch (α), GA (β), HS (γ), and tableted microcapsules (δ).

3.7 Encapsulation Efficiency

The EE and payload tests were directly carried out on freshly spray-dried HS-entrapping microcapsules with a spherical shape obtained following the procedure at 1000 rpm. The EE and payload values were determined to be 47±11% and 40±7%, respectively. With regards to the results obtained, it could be inferred that an aliquot of the HS dispensed in the formulation stage was either lost or unable to get encapsulated during the encapsulation process. This phenomenon might be due to the oil evaporation during the encapsulation stage, possible interactions between the chemicals, surface oil residues and oil leakage. However, similar values of EE (30-80%) for microcapsules achieved via CC were also reported in former literature [2, 27, 73, 80-82].

3.8 Release Profile

Oil release profile of microcapsules is primarily conditional upon the nature of the retained active ingredient interacting with the reticular shell complex. The composition of the dispersing medium also plays a key role. A water-based medium is the most typically used, but also cosolvent-enriched media may be employed if accelerated tests are required [5]. As can be seen in Figure 9, a time-dependent release of HS occurred from fCh-GA microcapsules when being exposed to aqueous environments. In water for a month, only <10% HS leakage was observed, which is very encouraging, and might result from the good barrier properties of solid coacervates being polymer-rich and, thus water-insoluble complexes [83, 84]. Meaningfully, this might explain the limited interference of surrounding water to act as a potential leakage-aid to the

microcapsules to release oil. When dealing with the long-term release, a typical exponential trend can be identified over the selected timeframe (>500 h). Overall, it could be deduced that aqueous environments may proactively contribute to determining the oil leakage rate of oil-entrapping microcapsules, thereby assessing their performance and barrier properties.

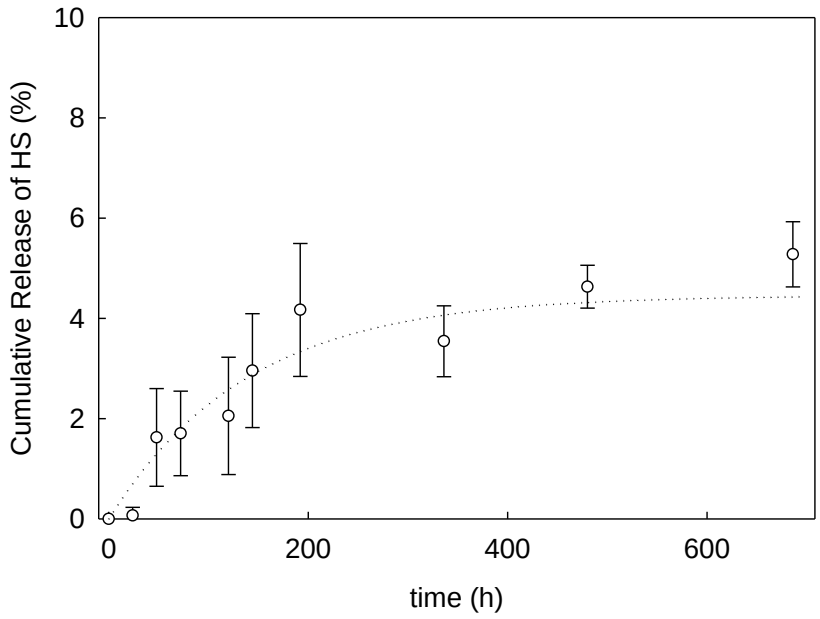

Figure 9 – Leakage profile of HS-microcapsules in water (◊). The dotted line displaying the trend of the release profile was fitted to a non-linear regression model (*i.e.* $y = a_{\lozenge}(1 - e^{-b_{\lozenge}t})$) based on the least squares analysis, with the corresponding evaluation of the coefficient of variation (CV (%) = St.Deviation/mean·10^2) using a software package (SigmaPlot 14.0, Systat Software Inc.). Relevant parameters including standard errors obtained: $a_{\lozenge} = 5.5 \pm 0.5$, $CV_{a\lozenge} = 9.0$ %, $b_{\lozenge} = 5.7 \cdot 10^{-3} \pm 1.2 \cdot 10^{-3}$ (h^{-1}), $CV_{b\lozenge} = 21.9$ %, $R^2 = 0.93$.

3.9 Rupture Force and Nominal Stress

A typical force *vs* displacement curve from compression of a single randomly chosen microcapsule is shown in Figure 10. Points α to β correspond to the progressive compression of a microcapsule which has been imaged as a built-in picture of Figure 10. Specifically, the α-β sequence shows an intact capsule before (α) being compressed following to the increasing force exerted by a descending probe onto the surface of the microcapsule itself. This results in a flattened-up coacervate structure from which the oil leaked out. A couple of oil residues aside are also shown (β). In addition, a clear depletion of the force applied is evident at point β, which is due to the sudden burst of the microcapsule. Accordingly, the threshold rupture force (F_r) of the selected microsphere can be determined. The nominal rupture stress (σ) and the nominal strain at rupture (%)

of each microcapsules defined as the ratio of the rupture force to its initial cross-sectional area, and the ratio of the displacement at rupture to original diameter, respectively [85], have been calculated.

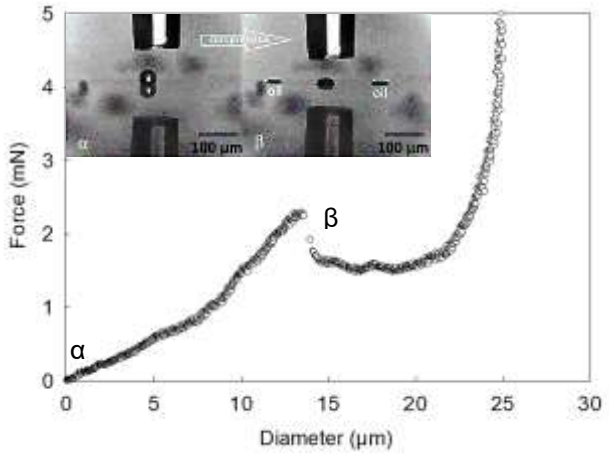

Figure 10 – Typical force *versus* displacement curve obtained from compression of a 40 μm microcapsule along with real-time pictures of its onset of compression (α), to its rupture point (β). A video showing the compression of a single HS-microcapsule *via* micromanipulation can be found in the electronic version of this article.

The rupture force of HS-entrapping microcapsules was found to be averagely increasing with diameter (Figure 11A), which is in good agreement with the results previously attained from melamine-formaldehyde (MF) microcapsules [85-87]. As displayed in Figure 11B the nominal rupture stress was found to be decreasing with the diameter, highlighting that greater microcapsules may be weaker and more likely to be broken than the smaller ones [88, 89]. The displacement increased with the size of the microcapsule (Figure 11C). Basing on the results herein presented, there appears that the nominal strain at rupture (which can be straightforwardly obtained from the slope of the trendline in Figure 11C) did not change with the diameter significantly, with a mean value of 22.7 ± 1.5 %. This was found to be very similar to nominal strain obtained by Long *et al.* [89] from MF-microcapsules, equal to 24.8 ± 1.5 %. The mean values of the relevant mechanical property parameters of HS-microcapsules along with their standard error obtained by micromanipulation are listed in Table 1, in comparison with those of well-established MF-formulated microcapsules, which had been reported in former contributions.

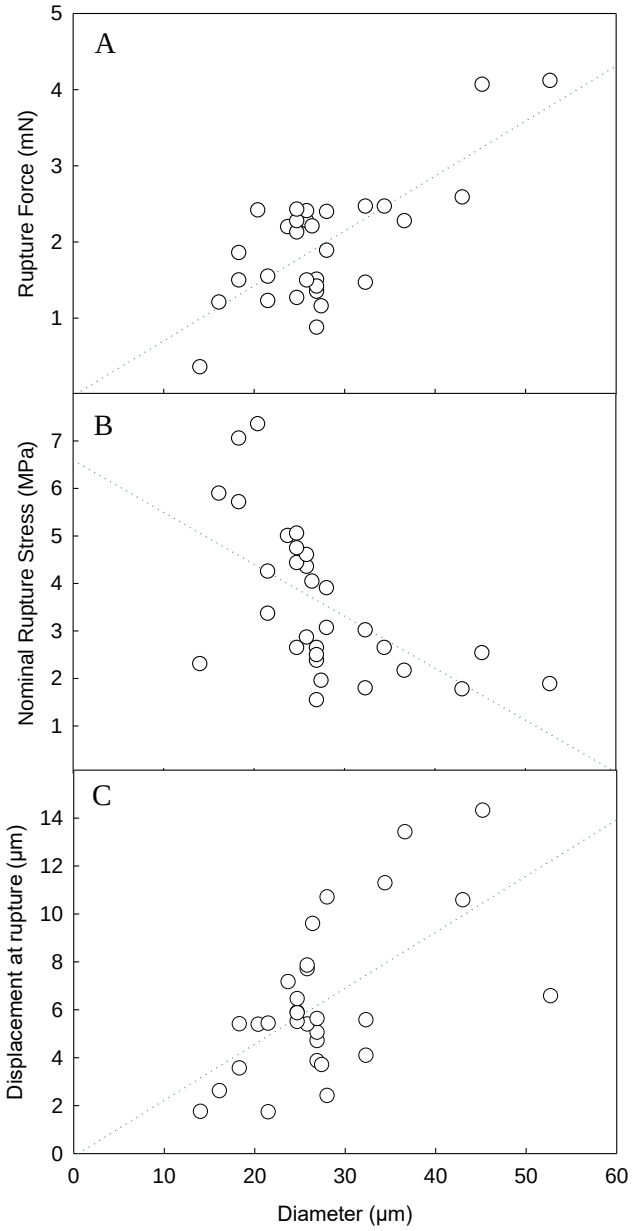

Figure 11 – Relevant trends of the mechanical properties of HS-entrapping microcapsules *vs* diameter (*d*): rupture force (A), nominal rupture stress (B), and displacement at rupture (C). The dotted lines only represent the trend.

TABLE 1: COMPARISON OF THE MECHANICAL PROPERTIES OF HS- ENTRAPPING MICROCAPSULES (MEAN ± ST.ERROR)

	fCh-GA caps	**MF caps**
Mean Diameter (μm)	27.5 ± 1.5	4.0 – 24.0 ± 1.0
Rupture Force (mN)	2.0 ± 0.1	0.7 ± 0.1 – 2.1 ± 0.2
Nominal Rupture stress (MPa)	3.6 ± 0.3	4.2 ± 0.4
Displacement at Rupture (μm)	6.3 ± 3.1	3.5 ± 0.2
Rupture Deformation (%)	22.7 ± 1.5	24.8 ± 1.5
Number of particles compressed	30	-
Reference	-	(Long et al., 2009b, 2016)

4. CONCLUSIONS

A theoretical-experimental CCCZ based on both NEC/zeta-potential (ζ-CCCZ) and turbidity (CTZ) studies was proposed to fabricate HS-entrapping microcapsules with an animal-free shell made of fCh and GA. CCCZ might be beneficially envisioned as an *a-priori* route for predicting suitable biopolyelectrolyte pairs to chemically react *via* CC. The highest EE of the microcapsules was found to be around 60%, which is similar to that previously reported for microcapsules made *via* CC from animal derived Ch and other biopolymers. It was found that the stirring rate set for CC affected the morphology of microcapsules, which appeared elongated and spherical at 400 and 1000 rpm, respectively. The experimental micromanipulation results highlighted that the rupture force of HS-entrapping microcapsules increased with the diameter, whereas the nominal rupture stress decreased with the size on average, as expected. It was also found that the nominal strain at rupture of such microcapsules did not change with the diameter significantly, with a mean value of 22.7±1.5 %. Conditionally upon the processing conditions (stirring speed 1000 rpm), the results elucidate that glutaraldehyde-crosslinked microcapsules with spherical shapes and micron-range sizes can be fabricated. Moreover, HS-entrapping microcapsules exhibited compact core-shell structures, and promising mechanical resistance (2.0 ± 0.1 mN). Overall, the employment of a fungal chitosan together with other safe plant-based materials to produce the shells of microcapsules may provide a new avenue to replace the current products on the market, which is currently relying on animal derivatives or non-biodegradable polymers. Future studies will address encapsulation of different oil-based active ingredients, guided by the established CCCZ.

GLOSSARY

ATR	Attenuated Total Reflection
CC	Complex Coacervation
CCCZ	Complex Coacervation Comfort Zone
Ch	Chitosan (animal derived)
CL	Crosslinking
CSS	Combined Stock Solution

CSSDU	Continuously Stirred Sample Dispersing Unit
CTZ	Critical Turbidity Zone
DI-w	Deionised water
EE	Encapsulation Efficiency
fCh	Fungal Chitosan
F_r	Threshold Rupture Force
FT-IR	Fourier Transform Infrared Spectroscopy
FTU	Formazine Turbidity Units
GA	Gum Arabic
Gl	Gelatine
Glu	Glutaric aldehyde
HS	Hexyl Salicylate
MWCO	Molecular Weight Cut-Off
o/w	Oil-in-water
NEC	Net electrokinetic charge
pH_{CC}	Optimum Complex Coacervation pH
PrOH	Propan-1-ol
QC	Quartz Crystal
RI	Refractive Index
SC	Simple Coacervation
SEI	Strength of Electrostatic Interaction
SEM	Scanning Electron Microscopy
TEA	Tri-Ethanol-Amine
TEM	Transmission Electron Microscopy
TV	Television
UV-Vis	Ultraviolet-Visible spectroscopy
VOC	Volatile Organic Compounds
ζ-CCCZ	NEC/Zeta potential based Complex Coacervation Comfort Zone
λ	Maximum absorbance wavelength
σ	Nominal Rupture Stress

CRediT AUTHORSHIP CONTRIBUTION STATEMENT

Dan Baiocco: Conceptualisation, Methodology, Validation, Investigation, Formal analysis, Data Curation, Visualisation, Writing - original draft.

Prof. Jon A. Preece: Conceptualisation, Visualisation, Supervision, Writing - review & editing.

Prof. Zhibing Zhang: Conceptualisation, Formal Analysis, Resources, Visualisation, Supervision, Writing - review & editing.

ACKNOWLEDGMENTS

The authors declaring no conflict of interest would like to thank the Engineering and Physical Sciences Research Council (EPSRC), UK & Lambson Ltd, UK for funding the project.

REFERENCES

1. Brain, J., et al., *Encapsulated Fragrance Chemicals.* US 7632789, 2009. **B2**.
2. Yang, Z., et al., *Development and evaluation of novel flavour microcapsules containing vanilla oil using complex coacervation approach.* Food Chem, 2014. **145**: p. 272-7.
3. Jun-xia, X., Y. Hai-yan, and Y. Jian, *Microencapsulation of sweet orange oil by complex coacervation with soybean protein isolate/gum Arabic.* Food Chemistry, 2011. **125**(4): p. 1267-1272.
4. Tekin, R., N. Bac, and H. Erdogmus, *Microencapsulation of Fragrance and Natural Volatile Oils for Application in Cosmetics, and Household Cleaning Products.* Macromolecular Symposia, 2013. **333**(1): p. 35-40.
5. Mercade-Prieto, R., et al., *Determination of the shell permeability of microcapsules with a core of oil-based active ingredient.* J Microencapsul, 2012. **29**(5): p. 463-74.
6. Mercadé-Prieto, R., et al., *Determination of the elastic properties of single microcapsules using micromanipulation and finite element modeling.* Chemical Engineering Science, 2011. **66**(10): p. 2042-2049.
7. Madene, A., et al., *Flavour encapsulation and controlled release - a review.* International Journal of Food Science and Technology, 2006. **41**(1): p. 1-21.
8. Rosca, I.D., F. Watari, and M. Uo, *Microparticle formation and its mechanism in single and double emulsion solvent evaporation.* Journal of Controlled Release, 2004. **99**(2): p. 271-280.
9. Busso, C.C., et al., *Glass transition temperatures and some physical and sensory changes in stored spray-dried encapsulated flavors.* Swiss Society of Food Science and Technology, 2007. **40**(10): p. 1792-1797.
10. Hwang, J.-S., et al., *Preparation and characterization of melamine-formaldehyde resin microcapsules containing fragrant oil.* Biotechnology and Bioprocess Engineering, 2006. **11**(4): p. 332-336.
11. Nunes, I.L. and A.Z. Mercadante, *Encapsulation of lycopene using spray-drying and molecular inclusion processes.* Brazilian Archives of Biology and Technology, 2007. **50**(5): p. 893-900.
12. Chen, A.C., M.F. Veigra, and B.R. Anthony, *Cocrystallization: an encapsulation process.* Food Technology, 1988. **42**(87–90).
13. Soper, J.C., D.K. Young, and M.T. Thomas, *Method of encapsulating flavors and fragrances by controlled water transport into microcapsules.* US Patent, 2000. **6106875**.
14. Gouin, S., *Microencapsulation: industrial appraisal of existing technologies and trends.* Trends in Food Science & Technology, 2004. **15**(7): p. 330-347.
15. Espinosa-Andrews, H., et al., *Gum Arabic-Chitosan Complex Coacervation.* Biomacromolecules 2007. **8**: p. 1313-1318.
16. De Kruif, C., F. Weinbreck, and R. de Vries, *Complex coacervation of proteins and anionic polysaccharides.* Current Opinion in Colloid & Interface Science, 2004. **9**: p. 340-349.
17. Sanchez, C., et al., *Self-Assembly of β-Lactoglobulin and Acacia Gum in Aqueous Solvent: Structure and Phase-Ordering Kinetics.* Langmuir, 2002. **18**(26): p. 10323-10333.
18. Weinbreck, F., R.H. Tromp, and C.G. De Kruif, *Composition and Structure of Whey Protein/Gum Arabic Coacervates.* Biomacromolecules 2004. **5**: p. 1437-1445.
19. Bungenberg de Jong, H.G.K., H. R. , *Coacervation (partial miscibility in colloid systems).* Proceedings of the Koninklijke Nederlandse Akademie der Wetenschappen, 1929. **32**: p. 849–856.
20. Dickinson, E. and V.B. Galazka, *Emulsifying Behaviour of Gum Arabic. Part 1: Effect of the Nature of the Oil Phase on the Emulsion Droplet-size Distribution.* Carbohydrate Polymers 1991. **14**: p. 373-383.
21. Luzzi, L.A. and R.J. Gerraughty, *Effects of selected variables on the extractability of oils from coacervate capsules.* Journal of Pharmaceutical Sciences, 1964. **53**(4): p. 429-431.
22. Prata, A.S. and C.R.F. Grosso, *Production of microparticles with gelatin and chitosan.* Carbohydrate Polymers, 2015. **116**: p. 292-299.
23. Huang, G.Q., et al., *Complex coacervation of soybean protein isolate and chitosan.* Food Chem, 2012. **135**(2): p. 534-9.
24. Elmer, C., et al., *Complex coacervation in pea protein isolate–chitosan mixtures.* Food Research International, 2011. **44**(5): p. 1441-1446.
25. Lee, A.-C. and Y.-H. Hong, *Coacervate formation of α-lactalbumin–chitosan and β-lactoglobulin–chitosan complexes.* Food Research International, 2009. **42**(5): p. 733-738.
26. Turgeon, S.L., C. Schmitt, and C. Sanchez, *Protein–polysaccharide complexes and coacervates.* Current Opinion in Colloid & Interface Science, 2007. **12**(4-5): p. 166-178.
27. Butstraen, C. and F. Salaün, *Preparation of microcapsules by complex coacervation of gum Arabic and chitosan.* Carbohydr Polym, 2014. **99**: p. 608-616.
28. Espinosa-Andrews, H., et al., *Interrelationship between the zeta potential and viscoelastic properties in coacervates complexes.* Carbohydr Polym, 2013. **95**(1): p. 161-6.
29. Ruphuy, G., et al., *Spray drying as a viable process to produce nano-hydroxyapatite/chitosan (n-HAp/CS) hybrid microparticles mimicking bone composition.* Advanced Powder Technology, 2016. **27**(2): p. 575-583.
30. Huang, G.-Q., et al., *Genipin-crosslinked O-carboxymethyl chitosan–gum Arabic coacervate as a pH-sensitive delivery system and microstructure characterization.* Journal of Biomaterials Applications, 2016. **31**(2): p. 193-204.
31. Gulão, E.d.S., et al., *Complex coacervates obtained from peptide leucine and gum arabic: Formation and characterization.* Food Chemistry, 2016. **194**: p. 680-686.
32. Assaf, S.A., G.O. Phillips, and P.A. Williams, *Studies on acacia exudate gums. Part I: the molecular weight of Acacia senegal gum exudate.* Food Hydrocolloids, 2005. **19**(4): p. 647-660.
33. Kim, K.M., et al., *Properties of Chitosan Films as a Function of pH and Solvent Type.* Journal of Food Science, 2006. **71**(3): p. E119-E124.
34. Jiang, T., et al., *Chitosan as a Biomaterial*, in *Natural and Synthetic Biomedical Polymers*. 2014. p. 91-113.
35. Hussain, M.R., M. Iman, and T. K. Maji, *Determination of Degree of Deacetylation of Chitosan and Their effect on the Release Behavior of Essential Oil from Chitosan and Chitosan Gelatin Complex Microcapsules.* International Journal of Advanced Engineering Applications, 2013. **2**(4): p. 4-12.
36. Chourpa, I., et al., *Conformational Modifications of α Gliadin and Globulin Proteins upon Complex Coacervates Formation with Gum Arabic as Studied by Raman Microspectroscopy.* Biomacromolecules, 2006. **7**(9): p. 2616-2623.
37. Maghsoudi, V., J. Razavi, and S. Yaghmaei, *Production of chitosan by submerged fermentation from aspergillus niger.* Scientia iranica, 2009. **16**(2 (transactions c: Chemistry chemical engineering)): p. 145-148.
38. Mint, A., et al., *N-acetylglucosamine/glucosamine copolymer capsules*, in *UK Patent Applications*, L. Limited, Editor. 2015: GB2542224-A.
39. Waibel, K.H., et al., *Safety of Chitosan Bandages in Shellfish Allergic Patients.* Military Medicine, 2011. **176**(10): p. 1153-1156.
40. Dhillon, G.S., et al., *Green synthesis approach: extraction of chitosan from fungus mycelia.* Critical Reviews in Biotechnology, 2013. **33**(4): p. 379-403.
41. Pochanavanich, P. and W. Suntornsuk, *Fungal chitosan production and its characterization.* Letters in Applied Microbiology, 2002. **35**(1): p. 17-21.
42. Varun, T.K., et al., *Extraction of chitosan and its oligomers from shrimp shell waste, their characterization and antimicrobial effect.* Veterinary world, 2017. **10**(2): p. 170-175.
43. Calabrese, R.V., T.P.K. Chang, and P.T. Dang, *Drop breakup in turbulent stirred-tank contactors. Part I: Effect of dispersed-phase viscosity.* AIChE Journal, 1986. **32**(4): p. 657-666.

44. Hu, J., H.-Q. Chen, and Z. Zhang, *Mechanical properties of melamine formaldehyde microcapsules for self-healing materials.* Materials Chemistry and Physics, 2009. **118**(1): p. 63-70.
45. Chang, Q., *Colloid and interface Chemistry for water quality control. Emulsion, Foam, and Gel.* . Academic Press, Inc., 2016: p. 227-245.
46. Poon, W.C.K., E.R. Weeks, and C.P. Royall, *On measuring colloidal volume fractions.* Soft Matter, 2012. **8**(1): p. 21-30.
47. Miller, J.F., *Determination of Protein Charge in Aqueous Solution Using Electrophoretic Light Scattering: A Critical Investigation of the Theoretical Fundamentals and Experimental Methodologies.* Langmuir, 2020. **36**(29): p. 8641-8654.
48. Pan, X., et al., *Structure and Mechanical Properties of Consumer-Friendly PMMA Microcapsules.* Industrial & Engineering Chemistry Research, 2013. **52**(33): p. 11253-11265.
49. Zhang, Z., R. Saunders, and C.R. Thomas, *Mechanical strength of single microcapsules determined by a novel micromanipulation technique.* Journal of microencapsulation, 1999. **16**(1): p. 117-124.
50. Liu, T., A.M. Donald, and Z. Zhang, *Novel manipulation in environmental scanning electron microscope for measuring mechanical properties of single nanoparticles.* Materials Science and Technology, 2005. **21**(3): p. 289-294.
51. Long, Y., et al., *Microcapsules with low content of formaldehyde: preparation and characterization.* Journal of Materials Chemistryv, 2009. **19**(37): p. 6882-6887.
52. Gray, A., et al., *Determination of microcapsule physicochemical, structural, and mechanical properties.* Particuology, 2016. **24**: p. 32-43.
53. Mano, J.F., G. Hungerford, and J.L. Gómez Ribelles, *Bioactive poly(L-lactic acid)-chitosan hybrid scaffolds.* Materials Science and Engineering: C, 2008. **28**(8): p. 1356-1365.
54. Claesson, P.M. and B.W. Ninham, *pH-dependent interactions between adsorbed chitosan layers.* Langmuir, 1992. **8**(5): p. 1406-1412.
55. Hudson, S.M. and D.W. Jenkins, *Chitin and Chitosan*. 2001, Encyclopedia of Polymer Science and Technology.
56. Padmanabhan, A. and L.S. Nair, *Chitosan hydrogels for regenerative engineering.* In: Dutta P. K, editor. Chitin and Chitosan for Regenerative Medicine, 2016. **New Delhi: Springers**: p. 3-40.
57. Matusiak, J., E. Grządka, and A. Bastrzyk, *Stability, adsorption and electrokinetic properties of the chitosan/silica system.* Colloids and Surfaces A: Physicochemical and Engineering Aspects, 2018. **554**: p. 245-252.
58. Lemetter, C.Y.G., F.M. Meeuse, and N.J. Zuidam, *Control of the morphology and the size of complex coacervate microcapsules during scale-up.* AIChE Journal, 2009. **55**(6): p. 1487-1496.
59. Atgié, M., O. Masbernat, and K. Roger, *Emulsions Stabilized by Gum Arabic: Composition and Packing within Interfacial Films.* Langmuir, 2019. **35**(4): p. 962-972.
60. Dong, D. and Y. Hua, *Glycinin-gum arabic complex formation: Turbidity measurement and charge neutralization analysis.* Food Research International, 2016. **89**: p. 709-715.
61. Dong, D., et al., *Charge Compensation, Phase Diagram, and Protein Aggregation in Soy Protein–Gum Arabic Complex Formation.* Journal of Agricultural and Food Chemistry, 2013. **61**(16): p. 3934-3940.
62. Jiménez-Alvarado, R.B., C. I.; Medina-Torres, L.; Román-Guerrero, A.; Vernon-Carter, E. J., *Ferrous bisglycinate content and release in W1/O/W2 multiple emulsions stabilized by protein–polysaccharide complexes.* Food Hydrocolloids, 2009. **23**(8): p. 2425-2433.
63. Weinbreck, F., *Theoretical description of CC.* 2004.
64. Vuillemin, M.E., et al., *Gum Arabic and chitosan self-assembly: Thermodynamic and mechanism aspects.* Food Hydrocolloids, 2019. **96**: p. 463-474.
65. Lechevallier, M.W., Evans T. M. , and J.S. Ramon, *Effect of Turbidity on Chlorination Efficiency and Bacterial Persistence in Drinking Water.* Applied and Environmental Microbiology, 1981. **42**(1): p. 159-167.
66. Davies-Colley, R.J. and D.G. Smith, *Turbidity Suspended Sediment and Water Clarity: a review.* Journal of the American Water Resources Association, 2001. **37**(5): p. 1085-1101.
67. Geng, X., O.-H. Kwon, and J. Jang, *Electrospinning of chitosan dissolved in concentrated acetic acid solution.* Biomaterials, 2005. **26**(27): p. 5427-5432.
68. Sogias, I.A., V.V. Khutoryanskiy, and A.C. Williams, *Exploring the Factors Affecting the Solubility of Chitosan in Water.* Macromolecular Chemistry and Physics, 2010. **211**(4): p. 426-433.
69. Lee, D.W., et al., *Strong Adhesion and Cohesion of Chitosan in Aqueous Solutions.* Langmuir, 2013. **29**(46): p. 14222-14229.
70. Kuck, L.S. and C.P.Z. Noreña, *Microencapsulation of grape (Vitis labrusca var. Bordo) skin phenolic extract using gum Arabic, polydextrose, and partially hydrolyzed guar gum as encapsulating agents.* Food Chemistry, 2016. **194**: p. 569-576.
71. Li, Q.-x., et al., *Electrolytic conductivity behaviors and solution conformations of chitosan in different acid solutions.* Carbohydrate Polymers, 2006. **63**(2): p. 272-282.
72. Farshchi, A., A. Hassanpour, and A.E. Bayly, *The structure of spray-dried detergent powders.* Powder Technology, 2019. **355**: p. 738-754.
73. Leclercq, S., K.R. Harlander, and G.A. Reineccius, *Formation and characterization of microcapsules by complex coacervation with liquid or solid aroma cores.* Flavour and Fragrance Journal, 2009. **24**(1): p. 17-24.
74. Espinosa-Andrews, H., et al., *Determination of the gum Arabic–chitosan interactions by Fourier Transform Infrared Spectroscopy and characterization of the microstructure and rheological features of their coacervates.* Carbohydrate Polymers, 2010. **79**(3): p. 541-546.
75. Qian, F., et al., *Chitosan Graft Copolymer Nanoparticles for Oral Protein Drug Delivery: Preparation and Characterization.* Biomacromolecules, 2006. **7**(10): p. 2722-2727.
76. Colthup, N.B., L.H. Daly, and S.E. & Wiberley, *Introduction to infrared and Raman spectroscopy.* Academic Press, Inc., 1990. **3rd ed.** : p. 319.
77. Alvarez-Ros, M.C., S. Sánchez-Cortés, and J.V. García-Ramos, *Vibrational study of the salicylate interaction with metallic ions and surfaces.* Spectrochimica Acta Part A: Molecular and Biomolecular Spectroscopy, 2000. **56**(12): p. 2471-2477.
78. Smith, B.C., *The C=O bond, Part VII: Aromatic Esters, Organic Carbonates, and more of the rule of three,.* Spectroscopy, 2018. **33**(9): p. 24-28.
79. Kildeeva, N.R., et al., *About mechanism of chitosan cross-linking with glutaraldehyde.* Russian Journal of Bioorganic Chemistry, 2009. **35**(3): p. 360-369.
80. Santos, M.G., et al., *Microencapsulation of xylitol by double emulsion followed by complex coacervation.* Food Chemistry, 2015. **171**: p. 32-39.
81. Ocak, B., *Film-forming ability of collagen hydrolysate extracted from leather solid wastes with chitosan.* Environmental Science and Pollution Research, 2018. **25**(5): p. 4643-4655.
82. Bruyninckx, K. and M. Dusselier, *Sustainable Chemistry Considerations for the Encapsulation of Volatile Compounds in Laundry-Type Applications.* ACS Sustainable Chemistry & Engineering, 2019. **7**(9): p. 8041-8054.
83. Stewart, R.J., C.S. Wang, and H. Shao, *Complex coacervates as a foundation for synthetic underwater adhesives.* Advances in colloid and interface science, 2011. **167**(1-2): p. 85-93.
84. Dompé, M., et al., *Underwater Adhesion of Multiresponsive Complex Coacervates.* Advanced Materials Interfaces, 2020. **7**(4): p. 1901785.
85. Yap, S.F., et al., *Understanding the Mechanical Properties of Single Micro-particles and their Compaction Behaviour.* China PARTICUOLOGY, 2006. **04**(01): p. 35-40.
86. Sun, G. and Z. Zhang, *Mechanical properties of melamine-formaldehyde microcapsules.* Journal of Microencapsulation, 2001. **18**(5): p. 593-602.
87. Zhang, Z., *Mechanical strength of single microcapsules determined by a novel micromanipulation technique.* Journal of Microencapsulation, 1999. **16**(1): p. 117-124.
88. Xue, J. and Z. Zhang, *Preparation and characterization of calcium-shellac spheres as a carrier of carbamide peroxide.* Journal of Microencapsulation, 2008. **25**(8): p. 523-530.
89. Long, Y., et al., *Microcapsules with low content of formaldehyde: preparation and characterization.* J. Mater. Chem., 2009. **19**(6882-6887).
90. Long, Y., et al., *Composite microcapsules with enhanced mechanical stability and reduced active ingredient leakage.* Particuology, 2016. **26**: p. 40-46.